Available online at www.sciencedirect.com
ScienceDirect
Trans. Nonferrous Met. Soc. China 35(2025) 800−818
Transactions of Nonferrous Metals Society of China
www.tnmsc.cn

Room temperature strengthening and quasi-superplasticity behavior in superlight Mg−3.11Li−2.31Al−1.95Sn−0.94Y−0.45Er alloy processed by multidirectional forging and asymmetric rolling

Fu-rong CAO[1,2], Nan-pan GUO[1], Pan-ning XU[1], Guang-ming XU[1]

1. School of Materials Science and Engineering, Northeastern University, Shenyang 110819, China;
2. State Key Laboratory of Rolling and Automation, Northeastern University, Shenyang 110819, China

Received 24 July 2023; accepted 26 February 2024

Abstract: To explore ambient strengthening and high temperature ductility, a combined forming approach of multidirectional forging and asymmetric rolling was proposed. A novel multicomponent ultralight Mg−3.11Li−2.31Al−1.95Sn−0.94Y−0.45Er alloy was fabricated. The microstructural evolution and mechanical properties were investigated by microstructural characterization and tensile test. The combined forming results in remarkable grain refinement. The ultimate tensile strength and elongation of (255±7) MPa and 24.9%, respectively, were obtained at room temperature. The contribution of various strengthening mechanisms of the rolled alloy was obtained. Microstructural examination revealed the occurrence of dynamic recrystallization at 473−573 K and dynamic grain growth at 573−623 K. The maximum elongation of 293.9% was demonstrated at 623 K and 5×10^{-4} s^{-1}. The dominate deformation mechanism at elevated temperatures is dislocation viscous glide.

Key words: Mg−Li−Al alloy; multidirectional forging; asymmetric rolling; microstructure; strengthening; superplasticity

1 Introduction

Due to the extremely low density, high specific stiffness, high specific strength, and good damping and electromagnetic shielding properties, Mg−Li alloys have the potential to gain applications in the aerospace, military, 3C electronic and automotive fields. Recent studies on Mg−Li alloys have attracted widespread attention [1]. The microstructures and properties of Mg−Li alloys were investigated extensively [2−7]. PENG et al [2,3] and LIANG et al [4] investigated the microstructure and mechanical properties of multicomponent Mg−Li alloys under different processing states. GAN et al [5] studied the dynamic recrystallization behavior of hot-compressed Mg−Li alloy. XU et al [6] and MA et al [7] investigated and reviewed the Mg−Li−Al composite and corrosion performance of Mg−Li alloys, respectively. According to the Mg−Li phase diagram [8], there are three phases: α (Li content <5.7 wt.%), $\alpha+\beta$ (Li content 5.7−10.3 wt.%) and β (Li content >10.3 wt.%). To reinforce the binary alloy, Al and Zn elements are usually added. Multiple ($\alpha+\beta$)-based [9] and β-based [10] alloys were thoroughly studied in the past, while the reports on the microstructures and properties of α-based Mg−Li alloy are still limited, especially in Mg−Li−Al series alloys. Therefore in this work, a new α-based multicomponent Mg−3Li−2Al−2Sn−1Y−0.5Er (in wt.%, hereinafter called LATY3221) alloy was designed. The addition of 3 wt.% Li was chosen to obtain α-based solid solution. 2 wt.% Al was added to achieve solid solution strengthening

Corresponding author: Fu-rong CAO, Tel: +86-15998161852, E-mail: cfr-lff@163.com, caofr@smm.neu.edu.cn
DOI: https://doi.org/10.1016/S1003-6326(24)66715-4

and secondary phase strengthening. 2 wt.% Sn was added to achieve solid solution strengthening and secondary phase strengthening. 1 wt.% Y was added to achieve grain refinement and secondary phase strengthening. 0.5 wt.% Er was added to achieve grain refinement and secondary phase strengthening. These are the reasons for choosing the Mg−3Li−2Al−2Sn−1Y−0.5Er alloy composition. It is necessary to study its microstructure and mechanical properties and improve the strength of the alloy to solve the problem of low strength of Mg−Li alloy. On the other hand, in recent years, Mg−Li alloy has been applied in the aerospace satellite manufacturing field in China. Because the temperature difference between day and night reaches 423 K in the lunar environment, it is necessary to study the high temperature properties of the alloy. At the same time, in order to make complex shape parts, it is essential to study superplasticity to solve the forming problem of complex parts. To this end, it is necessary to propose new forming method, study the microstructural evolution and mechanical properties, and investigate the room temperature strengthening mechanism and high temperature superplastic deformation mechanism.

Single severe plastic deformation method, such as ECAP (equal channel angular pressing) [11] and HPT (high-pressure torsion) [12], which refines the structure to improve the mechanical properties, has been extensively studied over the past thirty years. In recent years, a new combination forming has been developed into a new forming mode due to the limitations of single severe plastic deformation method. The multiple mode deformation or combined forming, such as rolling + ECAP [13], extrusion + HPT [14], extrusion + MDF (multi-directional forging) [15], rolling + CGP (constrained groove pressing) [16], extrusion + rolling [17], and so forth, is often seen in high quality reports. However, except that CAO's group used MDF + rolling (MDFR) combination forming to study superplasticity of (α+β)-based and β-based Mg−Li alloys [18,19] and investigated room temperature microstructure and properties [20], so far, there has been no report on the new α-based LATY3221 alloys fabricated by MDF + asymmetric rolling (AR). Therefore, the MDF + AR combination forming method was proposed to prepare LATY3221 alloy and study the microstructural evolution and mechanical properties of this alloy.

The mechanism of room temperature strengthening is an interesting topic, and the strengthening mechanism of Mg−Li alloy develops from qualitative research to quantitative research. Recently, the study on the strengthening mechanism has been increasing [21,22]. The purpose is, on the one hand, to clarify the contribution of various strengthening mechanisms [23], and on the other hand, to elucidate the strengthening mechanism from the microstructural characterization. However, according to our survey, there is no quantitative report on the strengthening mechanism in the present LATY3221 alloy. Thus, it is essential to fill this gap in such an alloy, gain an insight into the research of Mg−Li−Al−Sn−Y−Er alloy, and provide a fundamental understanding of the strengthening mechanism.

The high temperature superplasticity study is expected to improve the plasticity of LATY3221 alloy and create conditions for the forming of complex parts. Superplasticity is the ability of alloys to obtain large elongation at certain temperatures and strain rates with a grain size below 10 μm [24], usually typical superplasticity elongation greater than 400% and quasi-superplasticity elongation between 200% and 300%. KIM et al [25], FURUI et al [26], CHEN et al [27], and EDALATI et al [28] used differential speed rolling, ECAP and HPT in simple system Mg−Li alloys and obtained typical superplasticity. To the best of authors' knowledge, there are few reports on the superplasticity in multicomponent complex system Mg−Li alloy. Hence, the hot tensile microstructural evolution and superplasticity of LATY3221 alloy prepared by MDF + AR combination forming method need to be studied.

This paper includes four aspects. Firstly, the new LATY3221 alloy is prepared by MDF + AR combination forming method. Secondly, the microstructure and mechanical properties of LATY3221 alloy at room temperature and high temperature are studied. Thirdly, the physical strengthening models are used to study the room-temperature strengthening mechanisms. Fourthly, a power-law constitutive model is established to reveal the mechanism of high-temperature superplastic deformation.

2 Experimental

2.1 Alloy preparation

The raw materials used for the experiments were Mg, Al and Sn with purity greater than 99.9%, while Li, Y and Er elements were added with master alloys of Mg−20Li, Mg−20Y and Mg−30Er (in wt.%), respectively. All raw materials were put into a vacuum melting furnace according to the designed composition ratio and melted at 1053 K. Then, the molten metal was poured in a stainless steel mold and cooled under vacuum, and the ingot was obtained. The composition of the alloy was Mg−3.11Li−2.31Al−1.95Sn−0.94Y−0.45Er in wt.%. The prepared ingot was homogenized at 523 K for 16 h, and the ingot surface defects were milled and processed into a rectangular test block of 40 mm × 30 mm × 25 mm. The heating temperature of forging was 623 K and the holding time was 30 min. A hydraulic press was used for MDF along the three orthogonal directions of the test block. The schematic diagram of the MDF was shown in Ref. [20]. After each pass forging, the test block or cuboid was rotated 90° to continue forging. Forging three passes was a cycle. The forging cycle was repeated until all the set processes were completed. The reduction of each pass during forging was 37.5%, and the forged cuboid was water-quenched to room temperature to retain the hot forging microstructure. The LATY3221 alloy billet, forged for six passes, was heated to 673 K in the box type resistance furnace for 30 min, and was hot-rolled on the two-high AR mill. The differential speed ratio was 1:1.2, and the thickness change was 25→17→11→7→4→2 mm. The total reduction of AR was 23 mm, the total reduction was 92%, and the cumulative true strain was 2.527. After each rolling, the alloy plate should be intermediately heated at 673 K for 15 min.

2.2 Tensile tests

The sampling position of the tensile samples was in the bottom of the ingot and the central plane of the MDF cuboid. The rolled sample for tensile testing was machined along the rolling direction. The dog-bone shaped sample dimension for room temperature tensile testing was 10 mm in gauge length, 6 mm in width and 2 mm in thickness, as shown in Fig. 1(a). The tensile strain rate was 1×10^{-3} s^{-1}. Due to the small size of the test block, the tensile sample kept the gauge length unchanged after multidirectional forging, and the length of the holding part was correspondingly reduced to ensure enough clamping. The dog-bone shaped sample dimension for high temperature tensile testing was 6 mm in gauge length, 4 mm in width and 2 mm in thickness, as shown in Fig. 1(b). The samples shown in Fig. 1 were not standard samples. Each high temperature tensile test was done once. Due to the large number of tensile samples, two rolled sheets were selected for high temperature tensile experiments. The tensile tests at elevated temperatures were performed at a constant crosshead velocity in the temperature range of 473−623 K over strain rates of 1.67×10^{-2}–5×10^{-4} s^{-1} on a Shimidazu AG-XPLUS 100 kN tensile tester. After tensile tests, the samples for high temperature tests were quenched into water to reserve the microstructures at elevated temperatures.

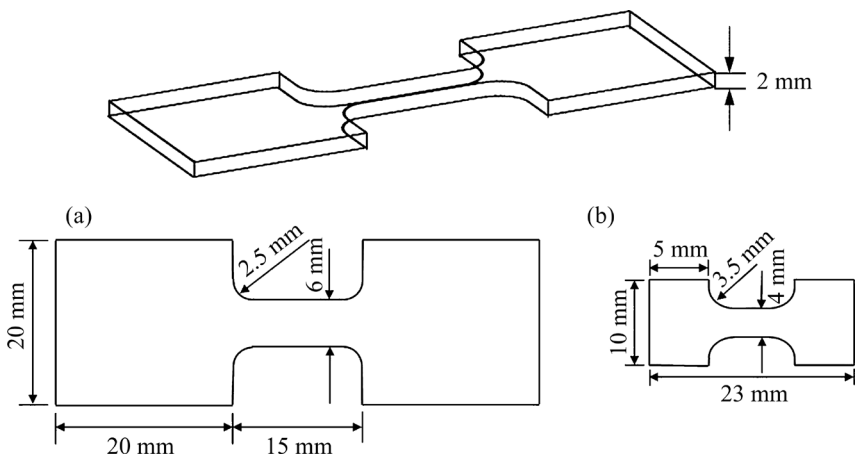

Fig. 1 Tensile sample dimensions: (a) Room temperature tension; (b) High temperature tension

2.3 Microstructural characterization

The optical examination sample of LATY3221 alloy was processed by mechanical polishing, coarse polishing and fine polishing. The sample surface was polished as bright as the mirror surface. The polished sample was then etched in a solution of 5 g picric acid + 5 mL acetic acid + 10 mL distilled water + 100 mL ethanol. The corrosion time was 25 s. Finally, an OLYMPUS microscope was used to obtain the required metallographic images. The average grain size and cavity radius were measured by Image Pro-Plus (IPP) software.

The qualitative and quantitative analysis of material phase composition was conducted on a Smartlab (9) X-ray diffractometer (XRD). The XRD phase test was performed for casting, MDF six-pass and asymmetrically rolled LATY3221 alloy samples. The phase composition of the alloy was analyzed using Jade 6 software.

The scanning electron microscope (SEM) for sample examination was a JSM−7001F field emission scanning electron microscope, with a resolution of 1.2 nm and a magnification of up to 500000 times. The types and contents of the microregion intermetallic compounds of the as-cast LATY3221 alloy were analyzed by an energy dispersive spectrometer (EDS).

3 Results

3.1 Microstructure and mechanical properties at room temperature

3.1.1 Microstructures at room temperature

Figure 2 shows the optical microstructures of LATY3221 alloy under different states. As can be seen from Fig. 2(a), there are several secondary phase particles in different shapes in the as-cast alloy. The optical microscope can identify the particle whose size is more than 1 μm. The matrix of the alloy is α-Mg solid solution phase with dense hexagonal close-packed (HCP) structure, the secondary phase agglomerates and grows at the grain boundary, and the size of the secondary phase particle is about 15 μm. The average grain size of the as-cast alloy is 271 μm. Figure 2(b) shows the metallographic structure of LATY3221 alloy after

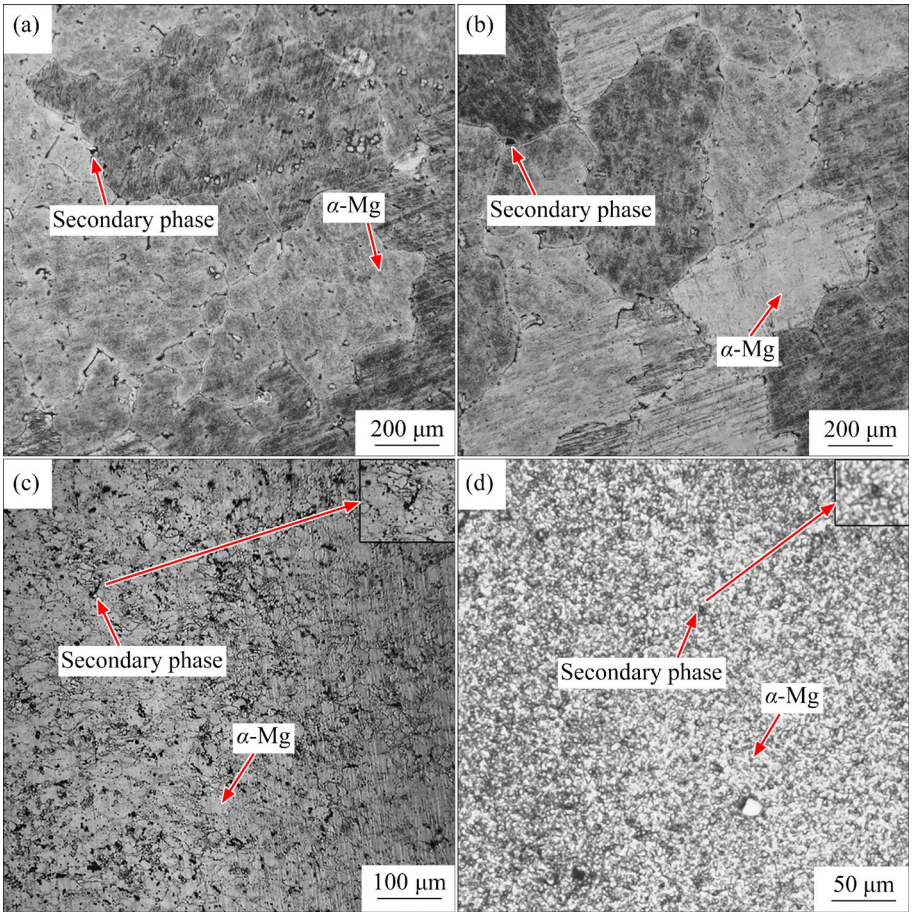

Fig. 2 Microstructures of LATY3221 alloys: (a) As-cast; (b) Homogenized at 523 K for 16 h; (c) Six-pass MDFed at 623 K (MDF-6); (d) Asymmetrically rolled at 673 K

homogenization at 523 K for 16 h. The grain size increases slightly, the average grain size is about 296 μm, and the number of secondary phase particles is significantly reduced due to the dissolution of particles in the matrix. As can be seen from Fig. 2(c), due to six-pass MDF deformation, fine secondary phase particles are broken and precipitated in the alloy, and the volume fraction of the secondary phase in the sixth pass is 9.76%. The secondary phase particles hinder the growth of grains during the hot deformation process and effectively refine the grains. Due to the MDF deformation, the average grain size is significantly reduced, and the grain distribution is more uniform. A greater degree of dynamic recrystallization occurs inside the alloy, the larger grains continue to be refined, and a large number of small dynamically recrystallized grains are evenly distributed around the large-size grains. As can be seen from Fig. 2(d), at the temperature of 673 K, along the rolling direction, the alloy is composed of fine grains, indicating that the grains are deformed and broken during the AR deformation. At the same time, a large number of small dynamically recrystallized grains are produced, and the grain distribution is more uniform. The grain microstructure of rolled alloy is obviously refined. The average grain size of the rolled alloy surface is (12.4±2.2) μm.

Figure 3 presents the X-ray diffraction patterns of LATY3221 alloy. It can be seen that after the alloy is treated by different processing processes, the phase type basically does not change, and the most important phase is the α-Mg matrix, while Mg_2Sn, AlLi and Al_2Y compounds and a small amount of Al_2Er intermetallic compound exist. The phase position and content of the samples at the MDF and AR states are basically the same, but the diffraction peak intensity of each phase is different. The microscopic morphology and phase composition of the LATY3221 alloy can be further observed and analyzed by using SEM and EDS.

Figure 4 presents the phase analysis results of LATY3221 alloy by means of SEM and EDS. It can be seen that in the as-cast LATY3221 alloy, the

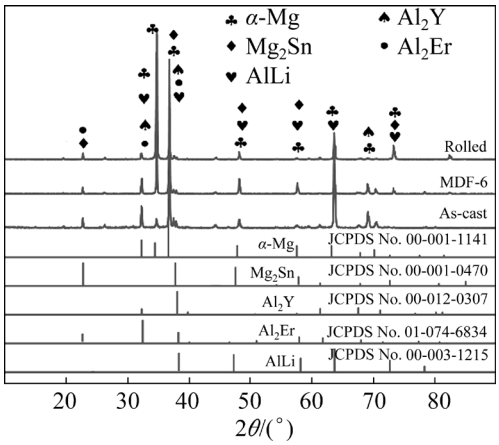

Fig. 3 XRD patterns of LATY3221 alloy

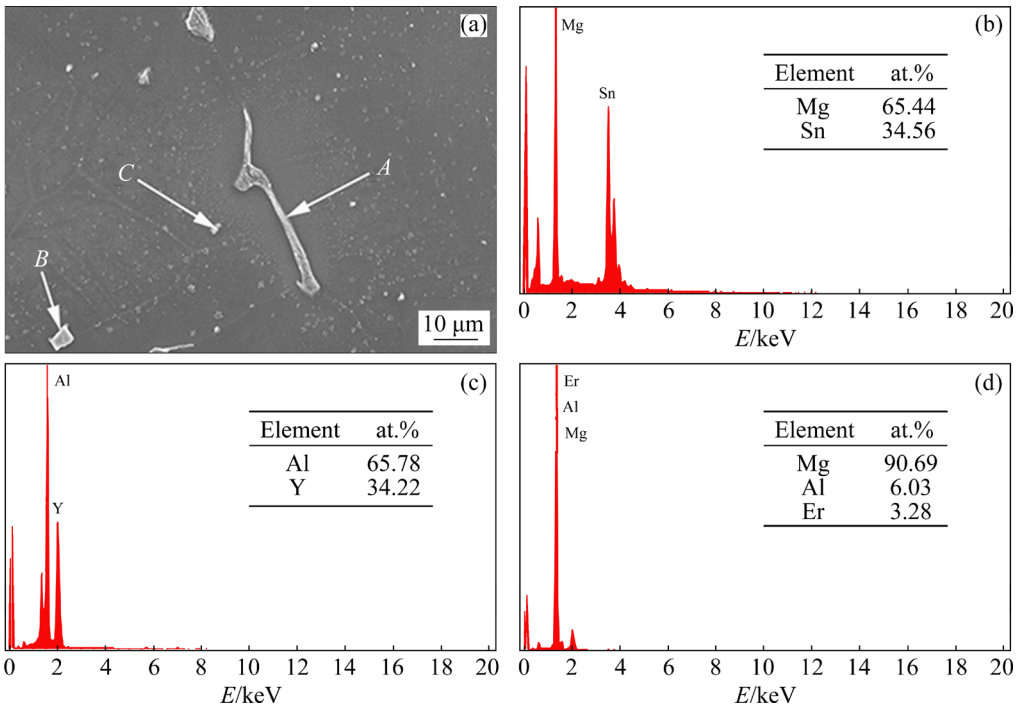

Fig. 4 Phase analysis results of as-cast LATY3221 alloy: (a) SEM image; (b) EDS results of Mg_2Sn; (c) EDS results of Al_2Y; (d) EDS results of Al_2Er

matrix is α-Mg, the rod phase is mainly distributed at the grain boundary, and the filament and gray block phases are distributed inside the grain. PENG et al [29] found that in the as-cast Mg−5Li−3Al−2Zn alloy, the AlLi phase formed a discontinuous network at the grain boundary. After the addition of Sn and Y elements, the irregular Mg_2Sn and the massive Al_2Y phase appeared. ZHOU et al [30] studied the microstructure and strengthening mechanism of extruded Mg−7Li−2Al−1.5Sn alloy and found that many short rod secondary phase precipitates of Mg_2Sn and Li_2MgSn were precipitated during the extrusion process, which effectively refined the dynamically recrystallized grains. These reports are consistent with the present EDS and XRD analysis of the LATY3221 alloy. Thus, based on Refs. [31,32], the rod phase at the grain boundary is identified as Mg_2Sn, the filament is identified as AlLi, and the bulk phase is identified as Al_2Y; the tiny black granular secondary phase is confirmed as the Al_2Er phase. Thus, based on above-mentioned evidence and experimental results in Fig. 4, the phase composition in the present alloy is composed of α-Mg solid solution phase and Mg_2Sn, AlLi, Al_2Y, and Al_2Er intermetallic compounds. This is consistent with the results of XRD analysis in Fig. 3. It is noted that EDS cannot detect Li elements, but the AlLi phase appears under the nonequilibrium solidification condition.

3.1.2 Mechanical properties at room temperature

Figure 5 shows the room temperature tensile curves and histograms of LATY3221 alloy under casting, homogenization, MDF, and AR conditions. Figure 5(a) shows the engineering stress−strain curves. It can be demonstrated from Figs. 5(a,c,d) that, the ultimate tensile strength (UTS), yield strength (YS), and elongation of the homogenized alloy all decreased relative to those of the as-cast alloy, and were (167±3) MPa, (106±2) MPa, and

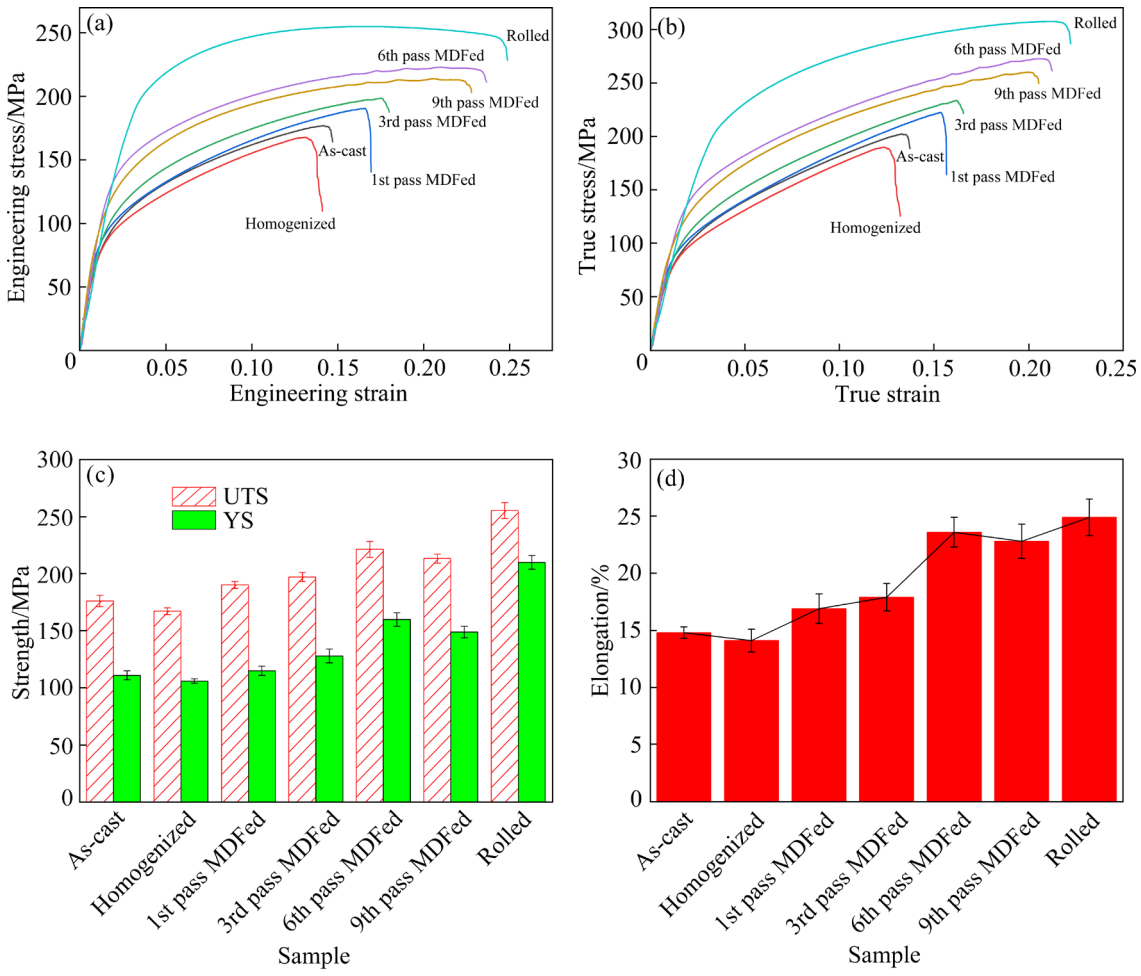

Fig. 5 Room temperature tensile curves and histograms of LATY3221 alloys: (a) Engineering stress−strain curves; (b) True stress−strain curves; (c) UTS and YS, and (d) Elongation under different treatment states

14.1%, respectively, mainly due to the slight increase of the grain size of the homogenized alloy, which caused the mechanical properties of the alloy to decrease. The UTS and elongation of the alloy increased significantly after MDF. At the first-pass MDF, the UTS, YS, and elongation of the alloy were (190±3) MPa, (115±4) MPa, and 16.9%, respectively, and the UTS increased by 13.8%. At the third-pass MDF, the UTS, YS, and elongation of this alloy were (197.1±4) MPa, (128±6) MPa, and 17.9%, respectively. As the cumulative strain increased, the UTS became larger. As a result, the UTS, YS, and elongation were (221±7) MPa, (160±6) MPa, and 23.6%, respectively, at the six-pass MDF. This indicated that the dynamic recrystallization and resulting grain refinement occurred during the MDF process, resulting in improved alloy properties. The UTS, YS, and elongation of the alloy after the ninth-pass forging were slightly reduced, and were (213±7) MPa, (149±6) MPa, and 22.8%, respectively. Perhaps, the repeated heating during the forging interval increased the atomic diffusion and resulted in the grain coarsening, which reduced the mechanical properties of the alloy. After the alloy undergoing six-pass MDF was subjected to the AR process, the UTS, YS, and elongation increased to (255±7) MPa, (220±6) MPa, and 24.9%, respectively, indicating that the MDF+AR process can significantly improve the strength of the alloy. This is due to the intense and severe shear strain accumulated by AR, which is more conducive to the dynamic recrystallization process and the generation of uniformly refined grains. Compared with Fig. 5(a) (engineering stress−strain curves), Fig. 5(b) shows the true stress−strain curves. The former is suitable for engineering design and analysis while the latter is suitable for theoretical analysis of strain-hardening or strain-softening. As can be seen from Fig. 5(b), the alloy has undergone the strain hardening process at room temperature, i.e., the flow stress curve shows an upward trend. True stress increases with the increase in true strain.

3.2 Microstructure and mechanical properties at elevated temperatures

3.2.1 Microstructures at elevated temperatures

Figure 6 shows the microstructures of the gauge section of LATY3221 alloy at different deformation temperatures of 473−623 K and initial strain rates of 1.67×10^{-2}–5×10^{-4} s^{-1}. Figure 7 shows the histograms of grain sizes of LATY3221 alloy pulled to failure at different temperatures and initial strain rates. As shown in Fig. 7, the grain sizes are in the range of 8.21−20.48 μm.

Figures 6(a_1−a_4) show the microstructures of the LATY3221 alloy at different strain rates at 473 K. As can be seen from Fig. 6(a_1), the strain rate is high and the temperature is low, the black secondary phase particles and grains are elongated along the tensile direction, and the average grain size is slightly reduced to 11.79 μm compared with the rolling state, indicating that the complete or full dynamic recrystallization (DRX) does not occur in the elongated grains, and the microstructure exhibits incomplete DRX. Compared with Fig. 6(a_1), the degree of the tensile deformation increases in Fig. 6(a_2), the number of fine DRX grains increases, and the average grain size decreases to 10.33 μm. With the continuous decrease of strain rate, the deformation time of the tensile sample is gradually extended. As can be seen from Fig. 6(a_3), the DRX degree further increases at this time, and a large number of small equiaxed grains appear, but some original rolled grains still exist, so the grains are refined to 8.48 μm. It can be seen from Fig. 6(a_4) that under the tensile strain rate of 5×10^{-4} s^{-1}, the tensile microstructure has undergone complete DRX, the grain distribution is relatively uniform, the grain refinement is obvious, and the average grain size decreases to 8.21 μm.

Figures 6(b_1−b_4) show the microstructures of the LATY3221 alloy at 523 K and different strain rates. Compared with Fig. 6(a_1), under the deformation temperature of 523 K and strain rate of 1.67×10^{-2} s^{-1} in Fig. 6(b_1), the degree of DRX at the tensile deformation site increases, the elongated deformed grains are changed into equiaxed grains, and the average grain size is slightly increased. As can be seen from Fig. 6(b_2), under the deformation conditions of 523 K and 5×10^{-3} s^{-1}, the DRX is basically completed, and a large number of equiaxed grains formed in the DRX process are evenly distributed in the tensile deformation site. As can be seen from Figs. 6(b_3, b_4), it is clear that the microstructure at the tensile deformation site of the alloy is mostly composed of DRX grains. Under the condition of long time holding, the growth phenomenon of some grains also appears, and most of the grains tend to be equiaxed.

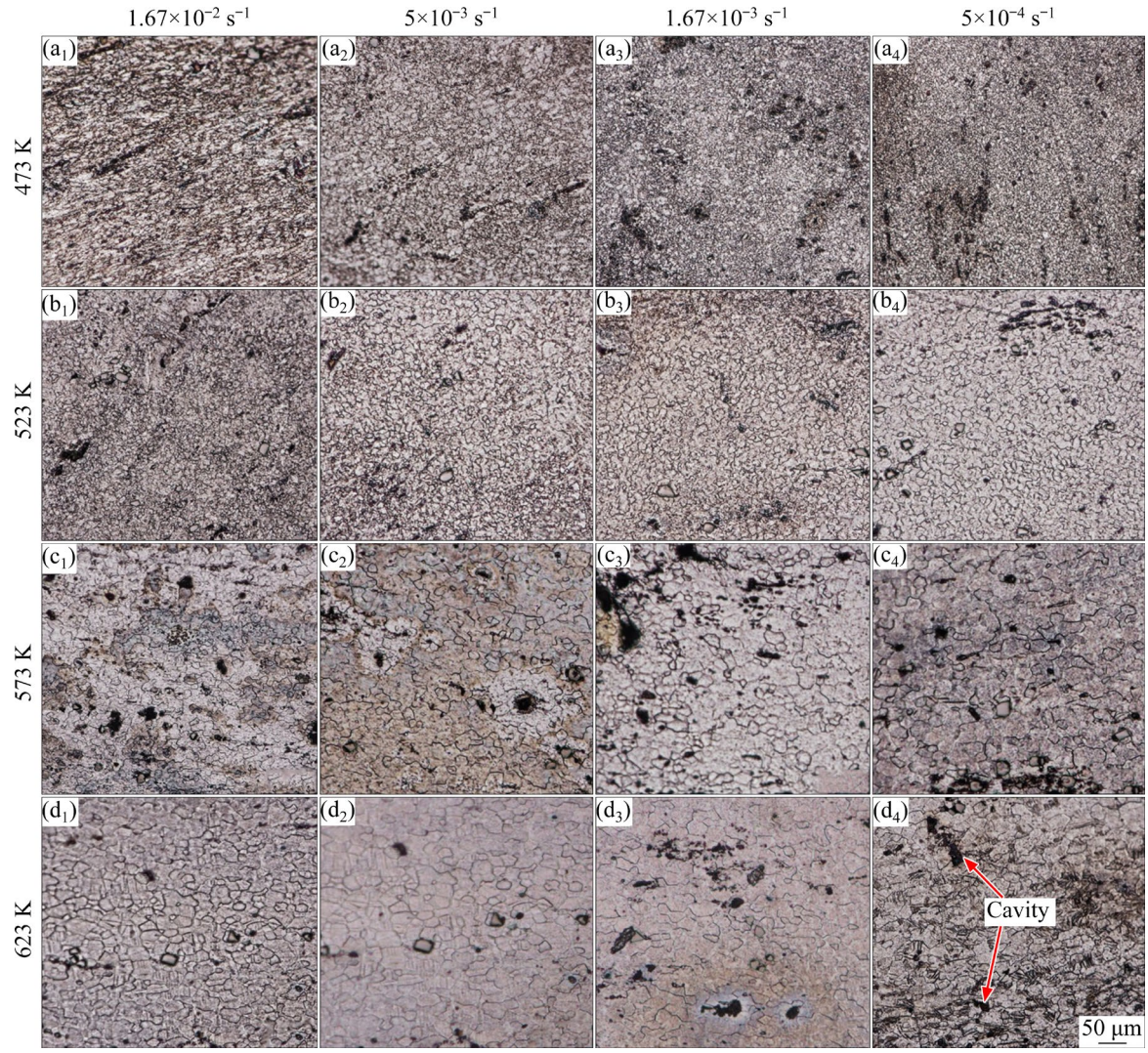

Fig. 6 Optical microphotographs of LATY3221 alloy on gauge section after deformation at different temperatures and initial strain rates

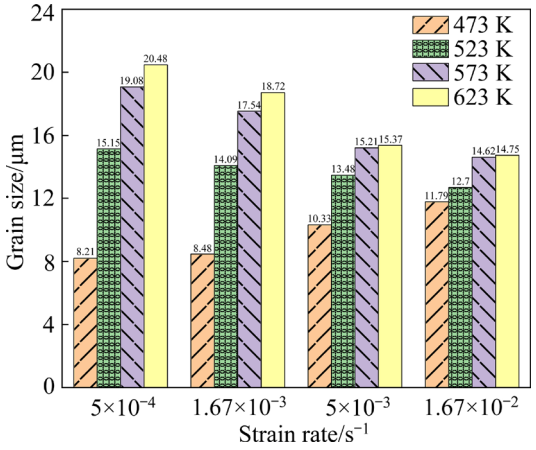

Fig. 7 Histograms of grain sizes in LATY3221 alloy pulled to failure at elevated temperatures

Figures 6(c_1−c_4) show the microstructures of the LATY3221 alloy at 573 K and different strain rates. Compared with Fig. 6(b_1), under the tensile deformation conditions of 573 K and 1.67×10^{-2} s^{-1} in Fig. 6(c_1), due to the high temperature and a short time deformation, the tensile site undergoes more DRX, producing a large number of equiaxed grains, accompanied by the growth of some fine grains. As can be seen from Fig. 6(c_1), near the white second phase particles, the cavity is more likely to produce around the secondary phase particles when the grain grows further. Figures 6(c_2, c_3) show that the grain size increases as the strain rate decreases. As can be seen from Fig. 6(c_4), with the decrease of strain rate, the cavity formed during the tensile process also expands with the grain growth.

Figures 6(d_1−d_4) show the microstructures of the LATY3221 alloy at 623 K and different strain rates. As can be seen from Figs. 6(d_1, d_2), at the

high strain rate, the alloy has completed the DRX process. Most of the microstructures at the tensile site are equiaxed grains, and the average grain size is significantly larger than that of the original grains in the rolling microstructure. As can be seen from Fig. 6(d_3), as the tensile deformation process proceeds, the equiaxed grains and cavities grow further. As can be seen from Fig. 6(d_4), due to the long time tensile deformation, the average grain size in the alloy grows to more than 20 μm, resulting in the decrease of deformation ability or thermal stability. Since dynamic grain growth results in strain hardening, the alloy elongation under this tensile condition finally reaches 293.9%.

In a word, in the process of high temperature tensile deformation, the DRX occurs in the tensile site during the tensile process. With the increase of temperature and the decrease of strain rate, the degree of DRX becomes larger, and the degree of grain growth in the tensile site becomes further larger after DRX. As shown in Figs. 6 and 7, DRX occurs in the temperature range of 473−573 K in most cases, whereas dynamic grain growth occurs in the temperature range of 573−623 K. Combined with the true stress−strain curve of Fig. 8, it can be determined that the microstructural evolution mechanism of the high-temperature tensile deformation in this alloy is mainly the DRX and the grain growth. In addition, the judging method of DRX or dynamic grain growth is presented here. Let $\Delta d = d' - d''$, where d' is initial grain size before tension, and d'' is the grain size after tension. The criterion is that if $\Delta d > 0$, DRX will occur, whereas if $\Delta d < 0$, dynamic grain growth will occur. For the judgement of DRX, an average grain size of d'=12.4 μm ((12.4±2.2) μm) is obtained from the rolled microstructure in Fig. 2(d). An average grain size of d''=8.21 μm is obtained from hot tensile microstructure in Fig. 6(a_4). $\Delta d = d' - d''$ = (12.4−8.21) μm = 4.19 μm > 0, indicating the occurrence of DRX. The same can be deduced by analogy.

3.2.2 Mechanical properties at elevated temperatures

Figure 8 shows the true stress−strain curves of the LATY3221 alloy at different temperatures and initial strain rates. The true stress of the alloy shows a decreasing trend with the decreasing strain rate.

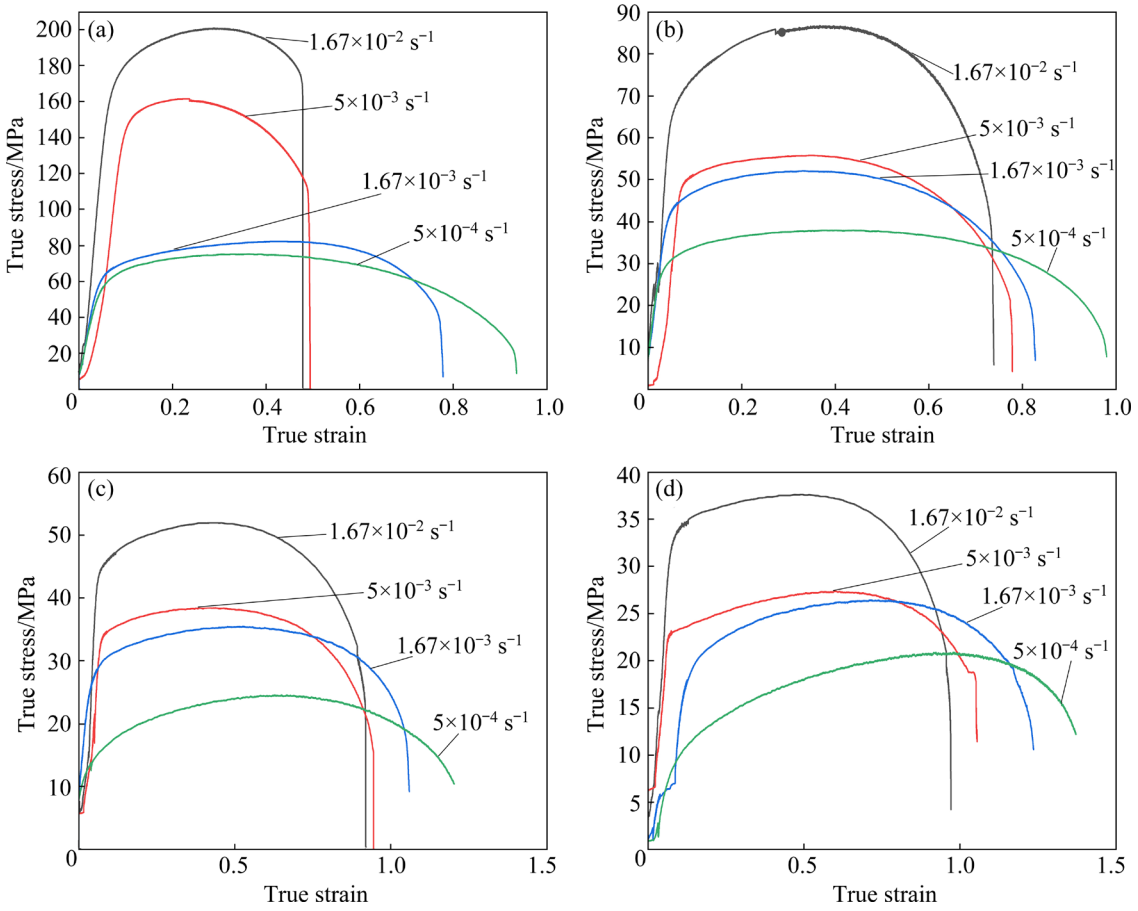

Fig. 8 True stress−strain curves of LATY3221 alloy at different temperatures and initial strain rates: (a) 473 K; (b) 523 K; (c) 573 K; (d) 623 K

The length of the flow platform becomes longer with increasing temperature and decreasing strain rate. As can be seen from Figs. 8(a−c), the flow stress increases with increasing the strain rate, because the strain hardening effect increases, and the deformation resistance increases when the strain rate increases. At low strain rate, heating time increases, DRX softens, and flow stress decreases. As can be seen from Fig. 8(d), in high temperature tension at the temperature of 623 K and initial strain rate of $5\times10^{-4}\ s^{-1}$, strain hardening stage occupies the most part, and strain softening stage is only a small part. This is because under a long time of high temperature holding, grain growing phenomenon that weakens the DRX softening effect leads to longer hardening stage and shorter softening stage, and reduces the high temperature plasticity of the alloy. The fact that the stress value of the high temperature stress−strain curve does not start from zero in Fig. 8 is related to the zero-point drift phenomenon of tensile tester and is caused by the overuse of tensile tester without enough maintenance. The fact that the slope of the elastic deformation stage of the same alloy does not coincide approximately in Fig. 8 is because the atomic vibration frequency is different at different tensile temperatures and strain rates under applied tensile load. Hence, different temperatures and strain rates correspond to different elastic deformation slopes. The elastic deformation stage of the curve at the temperature of 623 K and strain rate of $1.67\times10^{-3}\ s^{-1}$ has two turns, which may be related to higher atomic vibration frequency and zero-point drift.

Figure 9 presents the histograms of elongation in LATY3221 alloy after tensile deformation at elevated temperatures. Most elongations are in the range of 109.3%−293.9% with two exceptions of 61.3% and 67.2%. The elongations of 109.3%−293.9% indicate the enhanced ductility or quasi-superplasticity due to sufficient thermal activation. Two exceptions occur at lower temperature of 473 K, indicating that insufficient thermal activation occurs at this temperature and does not lead to the quasi-superplasticity. The maximum elongation of 293.9% is obtained at 623 K and $5\times10^{-4}\ s^{-1}$ and indicates superplasticity-like or quasi-superplasticity behavior in this coarse- grained alloy with a grain size of 20.48 μm, as shown in Fig. 6(d_4).

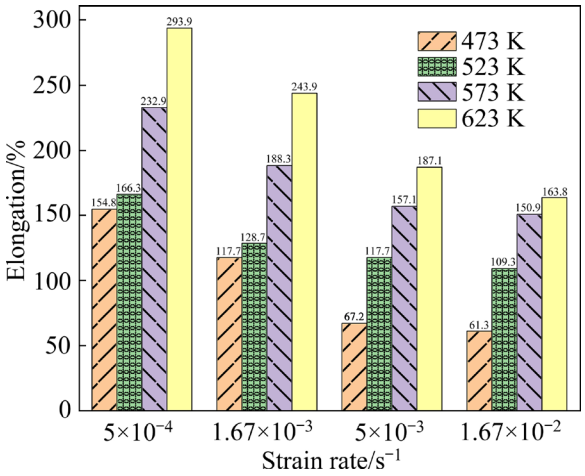

Fig. 9 Histograms of elongation of LATY3221 alloy pulled to failure at elevated temperatures

3.3 Modeling of power-law constitutive equation at elevated temperatures

To clarify the deformation mechanism at elevated temperatures, a power-law constitutive equation is established and is suitable for the application in hot deformation process and superplastic forming process. Power-law constitutive equation at elevated temperature is generally given as follows [33]:

$$\dot{\varepsilon}=\frac{AD_0Gb}{kT}\left(\frac{b}{d}\right)^p\left(\frac{\sigma-\sigma_{th}}{G}\right)^n\exp\left(-\frac{Q}{RT}\right) \quad (1)$$

where $\dot{\varepsilon}$ is the steady-state deformation rate, s^{-1}; A is a dimensionless constant; D_0 is the frequency factor for diffusion, m^2/s; G is the shear modulus (a function of temperature), MPa; b is the magnitude of Burgers vector of dislocation, m; k is Boltzmann constant, J/K; T is the thermodynamic temperature, K; d is the grain size, m; p is the grain size exponent; σ is the applied stress, MPa; σ_0 is the threshold stress, MPa; n (=1/m, m is strain rate sensitivity index) is the stress exponent; Q is the deformation activation energy, kJ/mol; R is the molar gas constant, J/(mol·K). Here, the n-, p-, and Q-values will be determined.

3.3.1 Stress exponent

Stress exponent, n, is related to threshold stress, σ_{th}. Threshold stress caused by the secondary phase particle is the onset stress to initiate the plastic flow. True stress at a true strain of 0.2 is chosen from the flow stress curves. Then, $\sigma-\dot{\varepsilon}^{1/2}$, $\sigma-\dot{\varepsilon}^{1/3}$, $\sigma-\dot{\varepsilon}^{1/4}$, and $\sigma-\dot{\varepsilon}^{1/5}$ curves are fitted linearly. The intercepts of the linear curves are the threshold

stresses, respectively. When σ_{th} value is positive and the fitting quality or correlation coefficient is the best, the corresponding n value is the optimal value.

Figure 10 presents the fitting curves of $\sigma-\dot{\varepsilon}^{1/2}$, $\sigma-\dot{\varepsilon}^{1/3}$, $\sigma-\dot{\varepsilon}^{1/4}$, and $\sigma-\dot{\varepsilon}^{1/5}$, respectively. The threshold stress is negative when n values are equal to 4 and 5. Thus, n=4 and 5 are excluded. When n values are equal to 2 and 3, it is found that fitting coefficient (R^2) value is the best at n=3. Hence, n=3 is the best true stress exponent or stress exponent.

3.3.2 Deformation activation energy

The true deformation activation energy, Q, at constant strain rate is expressed as the following relationship as per Eq. (1):

$$Q=R\left.\frac{\partial[\ln(\sigma^n G^{1-n}T^{-1}d^{-p})]}{\partial(T^{-1})}\right|_{\dot{\varepsilon}} \tag{2}$$

As n=3 quasi-superplasticity or dislocation viscous glide is dominant in this alloy, there exists p=0 [34].

The shear modulus, G, of pure Mg is given by the following relationship [35]:

$$\begin{cases} G=E/[2(1+\nu)] \\ E=48700-8.59T-0.0195T^2 \end{cases} \tag{3}$$

where Poisson ratio ν is equal to 0.35 [36].

Figure 11 shows the fitting curves of $\ln(\sigma^n G^{1-n}T^{-1})-T^{-1}$ at different strain rates. The deformation activation energy for LATY3221 alloy is in the range of 108.13−125.89 kJ/mol. The average activation energy is 116.8 kJ/mol. The diffusion coefficient can be expressed as

$$D=10^{-4}\exp[-116800/(RT)] \tag{4}$$

3.3.3 Normalized curve

Equation (1) is turned into the following form by taking logarithm:

$$\ln\left(\frac{\dot{\varepsilon}kT}{DGb}\right)=\ln A+n\ln\left(\frac{\sigma-\sigma_0}{G}\right) \tag{5}$$

Figure 12 shows fitting curve of $\ln[\dot{\varepsilon}kT/(DGb)]-\ln[(\sigma-\sigma_0)/G]$. The slope of the fitting line is 3.30 (≈3). The intercept of the fitting line is ln A (=15.09). Hence, A =3.57×10^6. The determination coefficient, R^2, is 0.91119, indicative of good correlation. Thus,

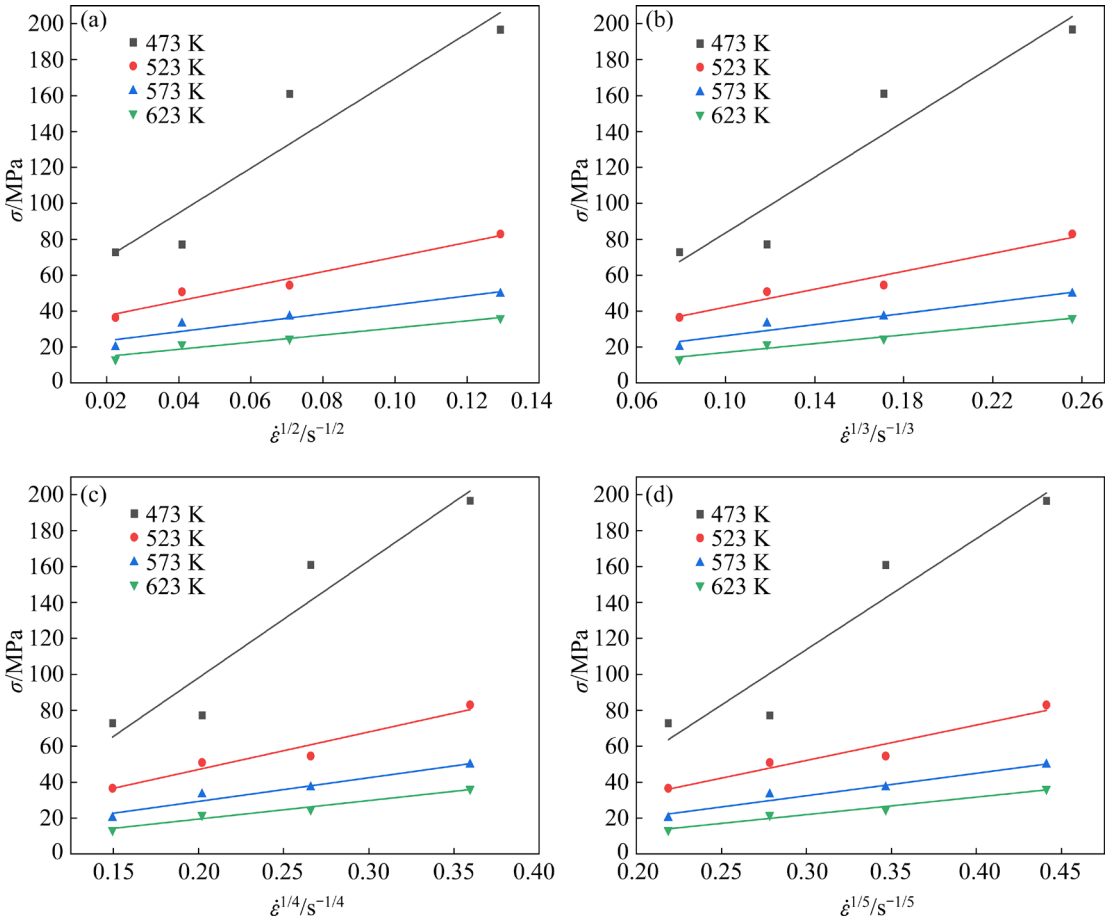

Fig. 10 Fitting curves of σ against $\dot{\varepsilon}^{1/n}$ for LATY3221 alloy: (a) n=2; (b) n=3; (c) n=4; (d) n=5

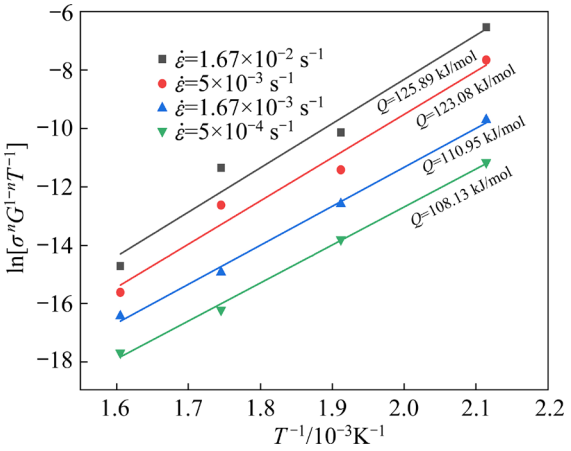

Fig. 11 Fitting curves of $\ln(\sigma^n G^{1-n} T^{-1})$–$T^{-1}$ for LATY3221 alloy at different strain rates

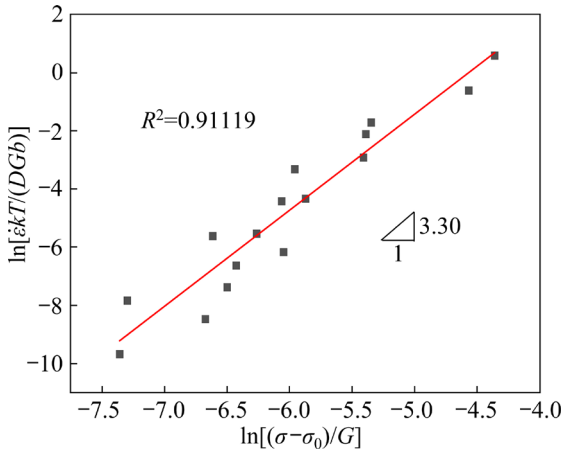

Fig. 12 Normalized curve of LATY3221 alloy

the power-law constitutive equation for LATY3221 alloy is obtained as follows:

$$\dot{\varepsilon} = 3.57\times10^{6}\frac{Gb}{kT}\left(\frac{\sigma-\sigma_0}{G}\right)^3 D \tag{6}$$

4 Discussion

4.1 Room-temperature strengthening in LATY3221 alloy

A qualitative analysis of the strengthening mechanisms is made for LATY3221 alloy. As shown in Section 3, LATY3221 alloy undergoes different processing stages of casting, homogenization, MDF, and AR. During alloying process, solutes like Li, Al, Sn, Y, and Er existing in the Mg matrix interact with dislocations, cause lattice distortion or strain, increase the resistance of dislocation movement in the lattice, and lead to solid solution strengthening. During MDF + AR processes, since grains are fragmented and refined and secondary phase particles are broken under applied stress, grain boundary strengthening and secondary phase strengthening occur. Meanwhile, due to severe plastic deformation, MDF + AR forming causes lattice misfit strain, increases dislocation activity such as dislocation multiplication and pile-up, increases the deformation resistance, and leads to strain hardening or dislocation strengthening. In a word, the interaction between dislocations and solutes, grain boundary, and secondary phase results in the alloy strengthening.

An estimation of the strengthening mechanisms using models and experimental data is made in this work. The strengthening yield strength of the alloy, σ_y, includes intrinsic stress, σ_0, dislocation strengthening stress, σ_d, grain boundary strengthening stress, σ_{gb}, solid solution strengthening stress, σ_{ss}, and secondary phase strengthening stress, σ_{Oro}, as shown in Eq. (7):

$$\sigma_y=\sigma_0+\sigma_d+\sigma_{gb}+\sigma_{ss}+\sigma_{Oro} \tag{7}$$

According to Fig. 5(a), the experimental yield strength of LATY3221 alloy is 220 MPa.

4.1.1 Contribution of intrinsic stress to yield strength

Intrinsic stress is the Peierls−Nabarro stress to impede dislocation movement on the slip plane. Intrinsic stress σ_0=11 MPa according to the stress range of 8−14 MPa [37]. Thus, the contribution of intrinsic stress to the yield strength is 5.00%.

4.1.2 Contribution of dislocation strengthening to yield strength

MDF + AR deformation induces a large number of dislocations, increases dislocation density, and leads to dislocation strengthening. The dislocation strengthening stress is given by [38]

$$\sigma_d=\alpha_d Gb\sqrt{\rho} \tag{8}$$

where α_d (=1.04) is a constant [38], ρ is the dislocation density of hot-rolled alloy, and shear modulus G is 16600 MPa at room temperature.

The dislocation density, ρ, is given by [39]

$$\rho=\frac{2\sqrt{3}\langle e^2\rangle^{1/2}}{bd'} \tag{9}$$

where d' is the coherent diffraction domain size, and e is the lattice strain.

As per our previous method to determine the dislocation density in flat hot-rolled plate of LAZY3330 alloy using XRD peak broadening [40]

and Fig. 3, d'=1.856 nm and e=0.0136 were obtained. Hence, $\rho=1.08\times10^{14}$ m^{-2} according to Eq. (9). The substitution of above-mentioned data into Eq. (8) gives σ_d=57.59 MPa. Thus, the contribution of dislocation strengthening to the yield strength is 26.18%.

4.1.3 Contribution of grain boundary strengthening to yield strength

MDF + AR deformation results in grain refinement. The grain refinement increases the number of grain boundary, leads to the pile-up and stress concentration of dislocations at the head of grain boundary, and increases the resistance to dislocation motion. Thus, grain boundary strengthening (Hall−Petch strengthening) occurs. Grain boundary strengthening stress is given by [38]

$$\sigma_{gb}=\alpha_{HP}G\sqrt{b/d} \tag{10}$$

where α_{HP}(=0.413) is a constant [38], and the grain size is 12.4 μm (Fig. 2(d)). Hence, σ_{gb}=34.88 MPa. Thus, the contribution of the grain boundary strengthening to the yield strength is 15.85%.

4.1.4 Contribution of solid solution strengthening to yield strength

In this alloy, solid solution strengthening results from the interaction between dislocations and solutes of Li, Al, Sn, Y, and Er elements inside the grain. This is because lattice misfit strain and associated distortion stress in the grain interior caused by the processing history hinder the dislocation motion and lead to the increment of yield strength. σ_{ss} is given by [41]

$$\sigma_{ss}=\sigma_{Mg}+(3.1\varepsilon Gc^{1/2})/700 \tag{11}$$

where σ_{Mg} (=21 MPa) is the yield stress of Mg single crystal [41], ε is the lattice distortion strain, $\varepsilon=(r_s-r_{Mg})/r_{Mg}$ (r_s is the atomic radius of solute, and r_{Mg} is the atomic radius of solvent), and c is the molar concentration of element. The substitution of the above-mentioned parameters into Eq. (11) gives σ_{ss}=24.72 MPa. Thus, the contribution of solid solution strengthening to the yield strength is 11.24%.

4.1.5 Contribution of secondary phase strengthening to yield strength

After MDF and AR deformation, the secondary phase particles are crushed into smaller particles, hinder the dislocation motion, and raise the strength. Secondary phase bypassing mechanism often prevails. Thus, secondary phase strengthening stress is obtained as per Eq. (7) as follows:

$$\sigma_{Oro}=\sigma_y-(\sigma_0+\sigma_d+\sigma_{gb}+\sigma_{ss}) \tag{12}$$

After above-mentioned data are substituted into Eq. (12), σ_{Oro}=91.81 MPa was obtained. Therefore, the contribution of secondary phase strengthening to the yield strength is 41.73%. This indicates that secondary phase strengthening makes a significant contribution to the yield strength. This reflects pronounced strengthening role of intermetallic compounds in this alloy.

A quantitative analysis of the contribution of various strengthening mechanisms is presented for this alloy. In terms of above-mentioned calculation, the following contribution of various strengthening mechanisms of the rolled alloy was obtained: secondary phase strengthening (41.73%), dislocation strengthening (26.18%), grain boundary strengthening (15.85%), solid solution strengthening (11.24%), and intrinsic lattice strengthening (5.00%). Firstly, the dislocation strengthening and grain boundary strengthening account for 42.03%, which indicates the significant role of MDF + AR deformation in enhancing the yield strength. Secondly, in this α-Mg phase based alloy, secondary phases such as Mg_2Sn, AlLi, Al_2Y, and Al_2Er exist. Secondary phase strengthening accounts for 41.73%, indicating the remarkable role of secondary phases in contribution to the yield strength. Thirdly, the contribution of the secondary phase particle strengthening, dislocation strengthening, and grain boundary strengthening accounts for 83.76% of the yield strength. This indicates that the dominant strengthening mechanism of LATY3221 alloy is the secondary phase strengthening, dislocation strengthening, and grain refinement strengthening. Fourthly, as per the available experimental yield strength of 111 MPa in as-cast state and 220 MPa in MDF + AR state, it is found that the yield strength in MDF + AR state is double that of as-cast state due to the imposed MDF + AR deformation. With the progress of processing process, the grain size changes from 271 to 12.4 μm while the secondary phase particles are significantly fragmented. Meanwhile, strain hardening or dislocation strengthening occurs. These evidences deepen our understanding of various strengthening mechanisms and demonstrate the scientific meaning and potential commercial significance of the present work.

4.2 Comparison of mechanical properties of available Mg−Li−Al alloys

The mechanical properties of available Mg−Li−Al alloys are compared. Figure 13 shows the comparison of the mechanical properties of available Mg−Li−Al alloys and depicts the recent research status of the mechanical properties of Mg−Li−Al series alloys [42−51]. It can be seen that the most common processing method of Mg−Li−Al alloy is extrusion, ternary Mg−Li−Al alloy accounts for a minority, and usually other alloy elements are added to further improve its mechanical properties. The elongation of Mg−Li−Al alloy is mostly concentrated in 10%−25%, and the UTS and YS are usually above 200 MPa. The past three years of research mainly focused on α+β duplex Mg−Li alloy made by extrusion [42−46,48,49] and other processing approaches [47,50,51]. Due to extrusion, the mechanical properties of Mg−Li−Al alloys are greatly improved, which provides a reference for the subsequent alloy composition design. The difference in the mechanical properties of Mg−Li−Al alloys studied by CAO et al [51] and the present work results from the difference in processing history. Higher UTS of 299.48 MPa in LAY720 alloy fabricated by flat rolling or symmetric rolling is due to strong cooling intensity during casting by water (as-cast grain size of 87 μm), heavy flat rolling reduction, and secondary phase, dislocation, and grain refinement strengthening, while intermediate UTS of 255 MPa in LATY3221 alloy fabricated by MDF + AR is due to lower cooling intensity during casting in air (as-cast grain size of 271 μm), heavy MDF + asymmetric rolling reduction, and secondary phase, dislocation, and grain refinement strengthening. This indicates that casting cooling mode and initial microstructures, including plastic forming history, have an important influence on the final mechanical properties. Compared with other Mg−Li−Al alloys, the advantage of ductility enhancement without deteriorating strength reflects the influence of grain refinement in the present alloy fabricated by MDF + AR. This indicates the impact of Hall−Petch grain refinement.

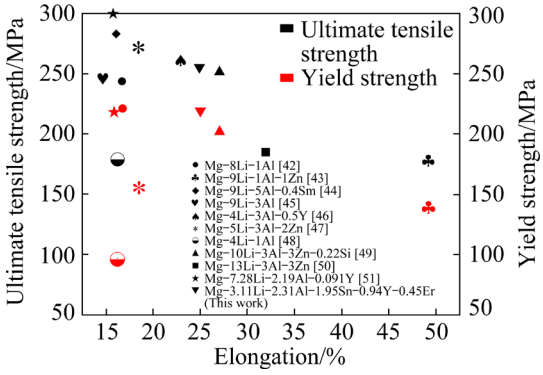

Fig. 13 Comparison of mechanical properties of available Mg−Li−Al alloys

The principle of combined forming of MDF + AR is proposed. This combined forming mode allows to cause large accumulative strain which is larger than the single strain of MDF or the single strain of AR. Also, compared with flat rolling or symmetric rolling, AR exerts more shear strain than flat rolling. Thus, the degree of AR grain refinement is larger than flat rolling grain refinement. As a result, the degree of grain refinement and secondary phase fragmentation is enhanced, and the mechanical properties are improved.

4.3 Quasi-superplasticity behavior and microstructure of LATY3221 alloy

According to Section 3.2, the hot tensile microstructural evolution and mechanical properties indicate DRX, dynamic grain growth, and cavity phenomena, which are quasi-superplastic behavior.

Firstly, DRX occurs in the LATY3221 alloy during hot tensile process at 473−573 K. Since the stacking fault energy of Mg is lower than that of Al, Mg alloy is prone to DRX. It is generally recognized that continuous DRX usually occurs during the hot tensile process, as demonstrated by MOHRI et al [52] in the superplastic AZ91 magnesium alloy. The continuous DRX process absorbs the dislocations and undergoes transition of the low-angle grain boundary to the high-angle grain boundary. Whether discontinuous DRX occurs in this alloy can be predicted or determined by using DERBY's formula [53]. DERBY [53] believes that discontinuous DRX obeys the following relationship:

$$\frac{\sigma}{G}\left(\frac{d}{b}\right)^{2/3}=K \tag{13}$$

where K is a constant, at 573 K and $5\times10^{-4}\,s^{-1}$, σ=25 MPa (Fig. 8(c)), G=13842.78 MPa (Eq. (3)), d=19.08 μm (Fig. 7), and b=3.21×10^{-10} m [54]. Substituting the above data into Eq. (13) gives K=2.85. This value falls into the range of normalized K values of 1−10 [53], indicating that

discontinuous DRX occurs under this condition. Thus, it is suggested that continuous DRX and discontinuous DRX occur in the present alloy. Therefore, DRX occurrence in this alloy at tensile temperatures of 473−573 K is consistent with the literature [53] and model predictions.

Secondly, dynamic grain growth appears in the LATY3221 alloy at tensile temperatures of 573−623 K. Previous studies [55−57] showed that ternary Mg−Zn−Zr (ZK 60) alloy and Mg−Li alloy had dynamic grain growth at 573−623 K. Mg_2Sn, AlLi, Al_2Y, and Al_2Er in complex LATY3221 alloy increase the DRX temperature of this alloy, prevent grain boundary migration to some extent, inhibit the dynamic grain growth at a temperature of 573 K (Fig. 8(c)), but due to the lattice diffusion and thermal activation acceleration at 623 K, the strain hardening in the flow stress curve is caused by the dynamic grain growth in Fig. 8(d). In this case, the maximum elongation is obtained at 623 K and 5×10^{-4} s^{-1}, which indicates superplasticity-like or quasi-superplasticity behavior in this coarse-grained alloy.

Thirdly, cavity appears in the LATY3221 alloy during the hot tensile process. The tensile fracture experiences cavity nucleation, growth, interlinkage, and fracture stage. The nucleation and growth of the cavity in Fig. 6 can absorb a large amount of strain energy during the tensile process, which is conducive to the further improvement of the elongation. The alloy yields 293.9% quasi-superplasticity at 623 K and 5×10^{-4} s^{-1}. According to Fig. 6(d_4), the percentage of the cavity nucleation and growth of the alloy is calculated to understand the mechanism of cavity evolution. CHOKSHI and MUKHERJEE [58] and CAO et al [59,60] proposed the following cavity nucleation models, respectively:

$$r_c(\text{Chokshi})=\left(\frac{\Omega D_l\sigma}{\pi kT\dot{\varepsilon}}\right)^{1/2} \tag{14}$$

$$r_c(\text{Cao})=5.2\left(\frac{\gamma}{\sigma}\right)\left(\frac{b}{d}\right)\left(\frac{G}{\sigma}\right) \tag{15}$$

where γ is the interface energy, Ω is the atomic volume, and D_l is the lattice diffusion coefficient. Substituting γ=1 J/m^2 [61], Ω==2.33×10^{-28} m^3 [54], $D_l=1.0\times10^{-4}\exp[-135000/(RT)]$ [54], G=13251.82 MPa (Eq. (3)), T=623 K, $\dot{\varepsilon}=5\times10^{-4}$ s^{-1}, σ=12 MPa (Fig. 8(d)), and d=12.4 μm (Fig. 2(d)) into the models in Eqs. (14) and (15) gives r_c(Chokshi)= 0.31 μm and r_c(Cao)=0.02 μm. Thus, r_c=0.165 μm. The experimental cavity radius in Fig. 6(d_4) is equal to r=2.78 μm. Therefore, the percentage of the cavity nucleation contribution is 5.93%; the percentage of the net cavity growth contribution is 94.07%. This suggests that cavity growth contributes the most to the cavity development.

4.4 Deformation mechanism of LATY3221 alloy at elevated temperatures

The theoretical grain boundary diffusion activation energy is 92 kJ/mol, and the lattice diffusion activation energy is 135 kJ/mol [54]. As per Section 3.3, the average experimental activation energy is 116.8 kJ/mol and is close to the theoretical activation energy of lattice diffusion, 135 kJ/mol. Thus, the diffusion mechanism is lattice diffusion. In the meantime, as per Section 3.3, the stress exponent is determined to be 3, indicating that dislocation viscous glide governs the rate-controlling process. The segregation of solutes around the dislocation creates a drag force that impedes dislocation motion [62]. Hence, solute-drag creep or dislocation viscous glide occurs. The stress exponent, n, in this case is 3 (m=0.33). The solute-drag creep or dislocation viscous glide mostly occurred in binary solid solution alloys at an early time and later extended to multicomponent solid solution based alloys. Available reports revealed the occurrence of dislocation viscous glide or solute drag creep resulting from the interaction of solutes and dislocations in solid solution based aluminum alloys and quasi-single phase magnesium alloys [63−65]. In the present alloy, the interaction of solutes like Li, Al, Sn, Y and Zr and dislocations leads to solute-drag creep or dislocation viscous glide. Thus, the deformation mechanism at elevated temperatures is dislocation viscous glide controlled by lattice diffusion.

To provide the theoretical evidence of dislocation activity, an estimation was made to calculate the number of dislocations inside a grain at 623 K and 5×10^{-4} s^{-1}. The number of dislocations inside a grain (N) is given by the following relationship [66]:

$$N=1.81(1-\nu)[d\sigma/(Gb)] \tag{16}$$

According to the data in Sections 3.3 and 4.3, N was estimated to be 41.15 (≈42). There are 42 pieces of dislocations inside a grain under this

condition. In addition, Eq. (16) was validated in our previous report [67] on hot-compressed Al−Mg−Er−Zr alloy and is convincing. Equation (16) stems from the modification of the model on dislocation balance in Ref. [68], not on solute-dislocation interaction. The dislocation distribution and number of dislocations in typical binary solid solution alloy in which solute-drag creep or dislocation viscous glide occurs are usually uniform and sparse and not many, but the number of dislocations is increased due to the obstruction of solute−dislocation interaction, and 42 pieces of dislocations exist inside a grain in this alloy. N=42 indicates the dislocation glide activity in the grain. So, the scientific significance of this calculation is to demonstrate the existence of positive dislocation activity. In consideration of aforementioned evidence, the deformation mechanism at elevated temperatures is found to be dislocation viscous glide controlled by lattice diffusion.

5 Conclusions

(1) A combined forming approach of MDF + asymmetric rolling was proposed. A novel α-Mg based multicomponent Mg−3.11Li−2.31Al−1.95Sn−0.94Y−0.45Er alloy was fabricated by this combined forming approach. The UTS, YS, and elongation of (255±7) MPa, (220±6) MPa, and 24.9%, respectively, were obtained at room temperature. The average grain size was changed from 217 μm in as-cast state to 12.4 μm in MDF + asymmetric rolling state, indicative of remarkable grain refinement. XRD and SEM−EDS examination revealed that the phase composition is composed of α-Mg solid solution phase and Mg_2Sn, AlLi, Al_2Y, and Al_2Er intermetallic compounds.

(2) As per the estimation by physical model, the following contribution of various strengthening mechanisms of the rolled alloy was obtained: secondary phase strengthening (41.73%), dislocation strengthening (26.18%), grain boundary strengthening (15.85%), solid solution strengthening (11.24%), and intrinsic lattice strengthening (5.00%). The dominant strengthening mechanism of LATY3221 alloy is the secondary phase strengthening, dislocation strengthening, and grain refinement strengthening.

(3) Microstructural examination revealed that the present alloy exhibits DRX at temperatures of 473−573 K, but dynamic grain growth at 573−623 K. Cavity phenomenon was observed, and cavity nucleation and net growth percentages were studied using models and experimental evidence. The maximum elongation of 293.9% was obtained at 623 K and 5×10^{-4} s^{-1}, which indicates superplasticity-like or quasi-superplasticity behavior in this coarse-grained alloy.

(4) A power-law constitutive equation was established. The stress exponent of 3 and deformation activation energy of 116.8 kJ/mol confirmed that the dominate deformation mechanism at elevated temperatures is dislocation viscous glide controlled by lattice diffusion.

CRediT authorship contribution statement

Fu-rong CAO: Conceptualization, Methodology, Writing − Original draft preparation, Review & editing, Formal analysis, Supervision; **Nan-pan GUO:** Conceptualization, Methodology, Investigation, Writing − Original draft preparation; **Pan-ning XU:** Visualization, Formal analysis, Data curation; **Guang-ming XU:** Writing − Review & editing, Formal analysis, Supervision.

Declaration of competing interest

The authors declare that they have no known competing financial interests or personal relationships that could have appeared to influence the work reported in this paper.

Acknowledgments

This work was supported by the National Natural Science Foundation of China (No. 51334006).

References

[1] GUO Yu-hang, HE Xuan-cheng, DAI Yi-bo, XIANG Hong-fu, ZANG Qian-hao, SHI Feng-jian, DONG Xu-guang, ZHANG Zhen-ya. Microstructures and mechanical properties of Mg−5Li−4Sn−2Al−1Zn alloy after hot extrusion [J]. Materials Science and Engineering A, 2022, 860: 144329.

[2] PENG Xiang, LIU Wen-cai, WU Guo-hua. Effects of Li content on microstructure and mechanical properties of as-cast Mg−xLi−3Al−2Zn−0.5Y alloys [J]. Transactions of Nonferrous Metals Society of China, 2022, 32(3): 838−849.

[3] PENG Xiang, SUN Jia-wei, LIU Hong-jie, WU Guo-hua, LIU Wen-cai. Microstructure and corrosion behavior of as-homogenized and as-extruded Mg−xLi−3Al−2Zn−0.5Y alloys (x=4, 8, 12) [J]. Transactions of Nonferrous Metals Society of China, 2022, 32(1): 134−146.

[4] LIANG Xin-li, PENG Xiang, JI Hao, LIU Wen-cai, WU Guo-hua, DING Wen-jiang. Microstructure and mechanical properties of as-cast and solid solution treated Mg−8Li−*x*Al−*y*Zn alloys [J]. Transactions of Nonferrous Metals Society of China, 2021, 31(4): 925−938.

[5] GAN Yi, HU Li, SHI Lai-xin, CHEN Qiang, LI Ming-ao, XIANG Lin, ZHOU Tao. Effect of AlLi phase on deformation behavior and dynamic recrystallization of Mg−Li alloy during hot compression [J]. Transactions of Nonferrous Metals Society of China, 2023, 33(5): 1373−1384.

[6] XU Lin, WANG Jia-hao, WU Rui-zhi, ZHANG Chun-bo, WU Hua-jie, HOU Le-gan, ZHANG Jing-huai. High specific strength MWCNTs/Mg−14Li−1Al composite prepared by electrophoretic deposition, friction stir processing and cold rolling [J]. Transactions of Nonferrous Metals Society of China, 2022, 32(12): 3914−3925.

[7] MA Xiao-chun, JIN Si-yuan, WU Rui-zhi, WANG Jia-xiu, WANG Gui-xiang, KRIT B, BETSOFEN S. Corrosion behavior of Mg−Li alloys: A review [J]. Transactions of Nonferrous Metals Society of China, 2021, 31(11): 3228−3254.

[8] NAYEB-HASHEMI A A, CLARK J B, PELTON A D. The Li−Mg (lithium−magnesium) system [J]. Bulletin of Alloy Phase Diagrams, 1984, 5: 365−374.

[9] SUN Yue-hua, WANG Ri-chu, PENG Chao-qun, WANG Xiao-feng. Effect of Gd on microstructure, mechanical properties, and corrosion behavior of as-homogenized Mg−8Li−3Al−2Zn−0.2Zr alloy [J]. Transactions of Nonferrous Metals Society of China, 2022, 32(8): 2494−2509.

[10] JI Qing, ZHANG Shun, WU Rui-zhi, JIN Si-yuan, ZHANG Jing-huai, HOU Le-gan. High strength BCC magnesium−lithium alloy processed by cryogenic rolling and room temperature rolling and its strengthening mechanisms [J]. Materials Characterization, 2022, 187: 111869.

[11] VALIEV R Z, STRAUMAL B, LANGDON T G. Using severe plastic deformation to produce nanostructured materials with superior properties [J]. Annual Review of Materials Research, 2022, 52: 357−382.

[12] LANGDON T G. Twenty-five years of ultrafine-grained materials: Achieving exceptional properties through grain refinement [J]. Acta Materialia, 2013, 61: 7035−7059.

[13] DEMIRTAS M, ATLI K C, YANAR H, PURCEK G. Enhancing the damping behavior of dilute Zn−0.3Al alloy by equal channel angular pressing [J]. Metallurgical and Materials Transactions A, 2017, 48: 2868−2876.

[14] TANG L L, ZHAO Y H, ISLAMGALIEV R K, VALIEV R Z, ZHU Y T. Microstructure and thermal stability of nano-crystalline Mg−Gd−Y−Zr alloy processed by high pressure torsion [J]. Journal of Alloys and Compounds, 2017, 721: 577−585.

[15] MIURA H, MATSUMOTO K, KOBAYASHI M. Micro-structure and mechanical properties of AZ61Mg alloy fabricated by multi-directional forging using die under decreasing temperature conditions [J]. Journal of the Japan Institute of Metals and Materials, 2015, 79(6): 295−302.

[16] FONG K S, DANNO A, TAN M J, CHUA B W. Tensile flow behavior of AZ31 magnesium alloy processed by severe plastic deformation and post-annealing at moderately high temperatures [J]. Journal of Materials Processing Technology, 2017, 246: 235−244.

[17] ZHANG T L, TOKUNAGA T, OHNO M, WU R Z, ZHANG M L, MATSUURA K. Low temperature superplasticity of a dual-phase Mg−Li−Zn alloy processed by a multi-mode deformation process[J]. Materials Science and Engineering A, 2018, 737: 61−68.

[18] CAO Fu-rong, XUE Guo-qiang, XU Guang-ming. Super-plasticity of a dual-phase-dominated Mg−Li−Al−Zn−Sr alloy processed by multidirectional forging and rolling [J]. Materials Science and Engineering A, 2017, 704: 360−374.

[19] CAO Fu-rong, SHANG Hui-hui, GUO Nan-pan, KONG Shu-ting, LIU Ren-jie. High strain rate quasi-superplasticity behavior in an ultralight Mg−9.55Li−2.92Al−0.027Y−0.026Mn alloy fabricated by multidirectional forging and asymmetrical rolling [J]. Materials, 2022, 15: 7539.

[20] CAO Fu-rong, ZHANG Jian, DING Xin, XUE Guo-qiang, LIU Si-yuan, SUN Chao-feng, SU Rui-kang, TENG Xiao-ming. Mechanical properties and microstructural evolution in a superlight Mg−6.4Li−3.6Zn−0.37Al−0.36Y alloy processed by multidirectional forging and rolling [J]. Materials Science and Engineering A, 2019, 760: 377−393.

[21] ZHA M, WANG S C, JIA H L, YANG Y, MA P K, WANG H Y. Effect of minor Ca addition on microstructure and mechanical properties of a low-alloyed Mg−Al−Zn−Sn alloy [J]. Materials Science and Engineering A, 2023, 862: 144457.

[22] ZHANG Z J, YUAN L, ZHENG M Y, WEI Q H, SHAN D B, GUO B. Achievement of high strength and good ductility in the large-size AZ80 Mg alloy using a designed multi-directional forging process and aging treatment [J]. Journal of Materials Processing Technology, 2023, 311: 117828.

[23] SUN X Y, WU D Y, KANG M J, RAMESH K T, KECSKES L J. Properties and hardening behavior of equal channel angular extrusion processed Mg−Al binary alloys [J]. Materials Characterization, 2023, 195: 112514.

[24] LANGDON T G. Seventy-five years of superplasticity: Historic developments and new opportunities [J]. Journal of Materials Science, 2009, 44: 5998−6010.

[25] KIM W J, KIM M J, WANG J Y. Ultrafine-grained Mg−9Li−1Zn alloy sheets exhibiting low temperature superplasticity [J]. Materials Science and Engineering A, 2009, 516: 17−22.

[26] FURUI M, KITAMURA H., ANADA H., LANGDON T G. Influence of preliminary extrusion conditions on the superplastic properties of a magnesium alloy processed by ECAP [J]. Acta Materialia, 2007, 55: 1083−1091.

[27] CHEN D X, KONG J, GUI Z Z, LI W, LONG Y, KANG Z.X. High-temperature superplastic behavior and ECAP deformation mechanism of two-phase Mg−Li alloy [J]. Materials Letters, 2021, 301: 130358.

[28] EDALATI K, MASUDA T, ARITA M, FURUI M, SAUVAGE X, HORITA Z, VALIEV R Z. Room-temperature superplasticity in an ultrafine-grained magnesium alloy [J]. Scientific Reports, 2017, 7: 2662.

[29] PENG X, XU S H, DING D H, LIAO G L, WU G H, LIU W C, DING W J. Microstructural evolution, mechanical properties and corrosion behavior of as-cast Mg−5Li−3Al−2Zn alloy with different Sn and Y addition [J]. Journal of

Materials Science & Technology, 2021, 72: 16−22.

[30] ZHOU G, YANG Y, ZHANG H Z, HU F P, ZHANG X P, WEN C, XIE W D, JIANG B, PENG X D, PAN F S. Microstructure and strengthening mechanism of hot-extruded ultralight Mg−Li−Al−Sn alloys with high strength [J]. Journal of Materials Science & Technology, 2022, 103: 186−196.

[31] HE Y Q, PENG C Q, FENG Y, WANG R C, ZHONG J F. Effects of alloying elements on the microstructure and corrosion behavior of Mg−Li−Al−Y alloys [J]. Journal of Alloys and Compounds, 2020, 834: 154344−154355.

[32] SUN Y, ZHANG M L, HAN W, LI M, YANG Y S, YAN Y D, ZHANG M. Electrochemical preparation of Mg−Li−Al−Er alloys by co-reduction in molten chloride [J]. Acta Metallurgica Sinica (English Letters), 2013, 26(4): 455−460.

[33] LANGDON T G. A unified approach to grain boundary sliding in creep and superplasticity [J]. Acta Metallurgica et Materialia, 1994, 42(7): 2437−2443.

[34] KASSNER M E, PÉREZ-PRADO M T. Five-power-law creep in single phase metals and alloys [J]. Progress in Materials Science, 2000, 45: 1−102.

[35] TALEFF E M, HECTOR L G, VERMA R, KRAJEWSKI P E, CHANG J K. Material models for simulation of superplastic Mg alloy sheet forming [J]. Journal of Materials Engineering and Performance, 2010, 19: 488−494.

[36] KANG Y H, WANG X X, ZHANG N, YAN H, CHEN R S. Effect of pre-deformation on microstructure and mechanical properties of WE43 magnesium alloy [J]. Materials Science and Engineering A, 2017, 689: 435−445.

[37] NAGARAJAN D, CACERES C H. The friction stress of the Hall−Petch relationship of pure Mg and solid solutions of Al, Zn, and Gd [J]. Metallurgical and Materials Transactions A, 2018, 49: 5288−5297.

[38] FERNANDEZ-ZELAIA P, MELKOTE S, MARUSICH T, USUI S. A microstructure sensitive grain boundary sliding and slip based constitutive model for machining of Ti−6Al−4V [J]. Mechanics of Materials, 2017, 109: 67−81.

[39] ZHAO Y H, LIAO X Z, JIN Z, VALIEV R Z, ZHU Y T. Microstructures and mechanical properties of ultrafine grained 7075 Al alloy processed by ECAP and their evolutions during annealing [J]. Acta Materialia, 2004, 52: 4589−4599.

[40] CAO Fu-rong, SUN Chao-feng, SHANG Hui-hui, XIANG Chao, LIU Ren-jie. Microstructure evolution and mechanical properties in an ultralight Mg−2.76Li−3Al−2.6Zn−0.39Y alloy [J]. Materials Science and Engineering A, 2021, 822: 141680.

[41] JIN X Z, XU W C, YANG G J, SHAN D B, GUO B. Microstructure evolution and strengthening mechanisms of Mg−6Gd−4Y−0.5Zn−0.5Zr alloy during hot spinning and aging treatment [J]. Materials Science and Engineering A, 2021, 827: 142035.

[42] ZHONG F, WU H J, JIAO Y L, WU R Z, ZHANG J H, HOU L G, ZHANG M L. Effect of Y and Ce on the microstructure, mechanical properties and anisotropy of as-rolled Mg−8Li−1Al alloy [J]. Journal of Materials Science & Technology, 2020, 39: 124−134.

[43] WU J Y, ZHAO D L, LEE B, ROY A, YAO R, CHEN S N, DONG Z Y, HEINEMAN W R, KUMTA P N. Effect of lithium and aluminum on the mechanical properties, in vivo and in vitro degradation, and toxicity of multiphase ultrahigh ductility Mg−Li−Al−Zn quaternary alloys for vascular stent application [J]. ACS Biomaterials Science & Engineering, 2020, 6(4): 1950−1964.

[44] HU Z, YIN Z, YIN Z, TANG B B, HUANG X, YAN H, SONG H G, LUO C, CHEN X H. Influence of Sm addition on microstructural and mechanical properties of as-extruded Mg−9Li−5Al alloy [J]. Journal of Alloys and Compounds, 2020, 842: 155836.

[45] DINESH P, KUMARESHBABU S P, NATARAJAN S. Effect of lanthanum addition on grain refinement and mechanical properties of Mg−9Li−3Al alloy [J]. Metals and Materials International, 2021, 27: 3993−4001.

[46] CHANG Li-li, GUO Jing, SU Xiao-jing. Effect of Y on microstructure evolution and mechanical properties of Mg−4Li−3Al alloys [J]. Transactions of Nonferrous Metals Society of China, 2021, 31(12): 3691−3702.

[47] LI X Q, REN L, LE Q C, BAO L, JIN P P, WANG P, CHENG C L, ZHOU X, HU C L. Reducing the yield asymmetry in Mg−5Li−3Al−2Zn alloy by hot-extrusion and multi-pass rolling [J]. Journal of Magnesium and Alloys, 2021, 9(3): 937−949.

[48] SHA G Y, LIU T, YIN M, NA Y D. The Portevin-Le Chatelier effect and strain-rate-induced plasticity enhancement in Mg−4Li and Mg−4Li−1Al alloys [J]. Materials Research Express, 2022, 9: 036514.

[49] SHEN Y Z, LI D F, GUO S L, GUO J T. Effect of heat treatment on microstructure and mechanical properties of Mg−10Li−3Al−3Zn−0.22Si alloy [J]. Metals and Materials International, 2022, 28: 2462−2471.

[50] YANG X H, JIN Y, WU R Z, WANG J H, WANG D, MA X C, HOU L G, SEREBRYANY V, TASHLYKOVA-BUSHKEVICH I I, BETSOFEN S Y. Simultaneous improvement of strength, ductility and damping capacity of single β-phase Mg−Li−Al−Zn alloys [J]. Metals, 2023, 13(1): 159.

[51] CAO Fu-rong, ZHOU Bi-jin, DING Xin, ZHANG Jian, XU Guang-ming. Mechanical properties and microstructural evolution in a superlight Mg−7.28Li−2.19Al−0.091Y alloy fabricated by rolling [J]. Journal of Alloys and Compounds, 2018, 745: 436−445.

[52] MOHRI T, MABUCHI M, NAKAMURA M, ASAHINA T, IWASAKI H, AIZAWA T, HIGASHI K. Microstructural evolution and superplasticity of rolled Mg−9Al−1Zn [J]. Materials Science and Engineering A, 2000, 290: 139−144.

[53] DERBY B. The dependence of grain size on stress during dynamic recrystallization [J]. Acta Metallurgica et Materialia, 1991, 39(5): 955−962.

[54] FROST H J, ASHBY M F. Deformation mechanism maps [M]. Oxford, UK: Pergamon Press, 1982: 21.

[55] KIM W J, LEE B H, LEE J B, LEE M J, PARK Y B. Synthesis of high-strain-rate superplastic magnesium alloy sheets using a high-ratio differential speed rolling technique [J]. Scripta Materialia, 2010, 63: 772−775.

[56] FIGUEIREDO R B, LANGDON T G. Factors influencing superplastic behavior in a magnesium ZK60 alloy processed by equal-channel angular pressing [J]. Materials Science and Engineering A, 2009, 503: 141−144.

[57] CAO F R, DING H, LI Y L, ZHOU G, CUI J Z. Superplasticity, dynamic grain growth and deformation mechanism in ultra-light two-phase magnesium−lithium alloys [J]. Materials Science and Engineering A, 2010, 527, 2335−2341.
[58] CHOKSHI A H, MUKHERJEE A K. An analysis of cavity nucleation in superplasticity [J]. Acta Metallurgica, 1989, 37(11): 3007−3017.
[59] CAO Fu-rong, LI Zhuo-liang, ZHANG Nian-xian, DING Hua, YU Fu-xiao, ZUO Liang. Superplasticity, flow and fracture mechanism in an Al−12.7Si−0.7Mg alloy [J]. Materials Science and Engineering A, 2013, 571: 167−183.
[60] CAO Fu-rong, ZHOU Bi-jin, YIN Bin, XUE Guo-qiang, ZHU Xiao-tong, XU Guang-ming. Modeling of deformation energy at elevated temperatures and its application in Mg−Li−Al−Y alloy [J]. Transactions of Nonferrous Metals Society of China, 2017, 27(11): 2434−2442.
[61] CHOKSHI A H. Cavity nucleation and growth in superplasticity [J]. Materials Science and Engineering A, 2005, 410/411: 95−99.
[62] JEONG H T, PARK H K, KANG H S, KIM W J. Operation of solute-drag creep in an AlCoCrFeMnNi high-entropy alloy and enhanced hot workability [J]. Journal of Alloys and Compounds, 2020, 824: 153829.
[63] YAVARI P, LANGDON T G. An examination of the breakdown in creep by viscous glide in solid solution alloys at high stress levels [J]. Acta Metallurgica, 1982, 30(12): 2181−2196.
[64] SHERBY O D, WADSWORTH J. Superplasticity: Recent advances and future directions [J]. Progress in Materials Science, 1989, 33: 169−221.
[65] RUANO O A, ALVAREZ-LEAL M, OROZCO-CABALLERO A, CARREÑO F. Large elongations in WE54 magnesium alloy by solute-drag creep controlling the deformation behavior [J]. Materials Science and Engineering A, 2020, 791: 139757.
[66] CAO Fu-rong, XIA Fei, XUE Guo-qiang. Hot tensile deformation behavior and microstructural evolution of a Mg−9.3Li−1.79Al−1.61Zn alloy [J]. Materials & Design, 2016, 92: 44−57.
[67] CAO Fu-rong, YIN Bin, LIU Si-yuan, SHI Lu, WANG Shun-cheng, WEN Jing-lin. Microstructural evolution, flow stress and constitutive modeling of a novel Al−1.88Mg−0.18Sc−0.084Er alloy during hot compression [J]. Transactions of Nonferrous Metals Society of China, 2021, 31(1): 53−73.
[68] ESHELBY J D, FRANK F C, NABARRO F R N. XLI. The equilibrium of linear arrays of dislocations [J]. Philosophical Magazine, 1951, 42: 351−364.

多向锻造异步轧制制备超轻 Mg−3.11Li−2.31Al−1.95Sn−0.94Y−0.45Er 合金的室温强化与准超塑性行为

曹富荣[1,2]，郭楠盼[1]，徐潘宁[1]，许光明[1]

1. 东北大学 材料科学与工程学院，沈阳 110819；
2. 东北大学 轧制与连轧自动化国家重点实验室，沈阳 110819

摘　要：为了探索镁锂合金的室温强化与高温塑性，提出一种多向锻造与异步轧制组合成形方法。采用该方法制备了新型多元超轻 Mg−3.11Li−2.31Al−1.95Sn−0.94Y−0.45Er 合金。采用显微组织表征和拉伸测试研究了合金的显微组织与力学性能。经过该组合成形，合金发生显著晶粒细化。室温获得的极限抗拉强度与伸长率分别为(255±7) MPa 与 24.9%。获得了轧制合金各种强化机理的贡献。显微组织观察发现，合金在 473~573 K 发生动态再结晶，在 573~623 K 发生动态晶粒生长。在 623 K 和 5×10^{-4} s^{-1} 条件下获得了 293.9%的最大伸长率。主导合金高温变形的机理为位错黏性滑移。

关键词：Mg−Li−Al 合金；多向锻造；异步轧制；显微组织；强化；超塑性

(Edited by Wei-ping CHEN)